A&A 468, 221–231 (2007)
DOI: 10.1051/0004-6361:20066229

Astronomy & Astrophysics

Simultaneous *XMM-Newton* and VLT/UVES observations of the flare star CN Leonis[*]

B. Fuhrmeister, C. Liefke, and J. H. M. M. Schmitt

Hamburger Sternwarte, University of Hamburg, Gojenbergsweg 112, 21029 Hamburg, Germany
e-mail: `bfuhrmeister@hs.uni-hamburg.de`

Received 11 August 2006 / Accepted 23 January 2007

ABSTRACT

Aims. We present simultaneous observations with VLT/UVES and *XMM-Newton* of the active M5.5 dwarf CN Leo (Gl 406). The data were gathered during three half nights in May 2004 and December 2005, and they cover quiescent states, as well as flaring activity. Our main aim is to derive coronal properties from X-ray data and to compare these to results from the optical Fe XIII line.
Methods. We studied simultaneously-measured coronal and chromospheric parameters of CN Leo as determined from the *XMM-Newton* X-ray data, the forbidden optical coronal Fe XIII line at 3388 Å, and various optical chromospheric emission lines.
Results. We find that different activity levels of CN Leo can be traced as well in X-rays as with the Fe XIII line. Moreover, the Fe XIII line flux is in good agreement with a prediction using the differential emission measure as determined from the X-ray spectrum and Fe atomic data. We also present coronal X-ray properties for the quiescent and flaring states of CN Leo. During a flare two He II transition region lines are also detected in the optical data.

Key words. stars: activity – stars: late-type – stars: individual: CN Leo – stars: coronae – X-rays: stars

1. Introduction

CN Leo (Gl 406) is a well-known nearby flare star with a spectral type of M5.5 (Reid et al. 1995) or M6.0 (Kirkpatrick et al. 1991) at a distance of 2.39 pc (Henry et al. 2004). Using a fixed $\log g$ of 5.0 and solar metallicity, Pavlenko et al. (2006) find a $T_{\rm eff}$ of 2800 ± 100 K, while Fuhrmeister et al. (2005b) have fitted $\log g$ and $T_{\rm eff}$ simultaneously and determined $T_{\rm eff} = 2900$ K and $\log g = 5.5$ using a grid with $\Delta T_{\rm eff} = 100$ K and $\Delta \log g = 0.5$. Pavlenko et al. (2006) also determined $M_{\rm bol} = 12.13 \pm 0.1$, yielding an age of 0.1–0.35 Gyr and a mass of 0.07–0.1 $M_{\odot}$ for CN Leo. This relatively young age corresponds well with CN Leo's high activity level. Surprisingly, CN Leo has been kinematically classified as an old disk star by Mohanty & Basri (2003), which would (statistically) imply a higher age. Therefore, Pavlenko et al. conclude that CN Leo is a young disk star, falling outside the kinematic dispersion of the young disk population. Interestingly, despite its high activity level, a rather low rotational velocity of $v \sin i < 3.0$ km s^{-1} has been found by Mohanty & Basri (2003).

CN Leo's high activity levels manifest themselves in its high relative Hα luminosity of $\log L_{\rm H\alpha}/L_{\rm bol} = -3.89$, (Mohanty & Basri 2003), the multitude of chromospheric emission lines in its near ultraviolet spectrum (Fuhrmeister et al. 2004), and its high X-ray flux. The X-ray luminosity of CN Leo observed during the *ROSAT* All-Sky survey was $\log L_{\rm X} = 26.97$, while two pointed observations with the *ROSAT* PSPC yielded higher values of $\log L_{\rm X} = 27.01$ and 27.64 (Schmitt & Liefke 2004). Also, CN Leo is the only M dwarf for which persistent but variable emission of the forbidden coronal Fe XIII line at 3388 Å could be established (Schmitt & Wichmann 2001; Fuhrmeister et al. 2004), although several surveys among M dwarfs with high and low activity levels have been carried out. Fuhrmeister et al. report one additional clear detection for LHS 2076 during a major flare for a sample of 15 very active M3–M6.5 dwarfs, while Wallerstein & Tyagi (2004) find no Fe XIII emission in a sample of 8 M dwarfs with rather low activity levels. This apparent rarity of M dwarfs exhibiting the Fe XIII forbidden coronal line may be due to the different coronal temperature structure of active M dwarfs as compared to the Sun. Typical emission measure distributions of the coronae of M3–M4 dwarfs peak around 7–8 MK as determined with XMM-Newton (Robrade & Schmitt 2005), i.e., a temperature too hot for significant amounts of Fe XIII.

However, the X-ray luminosity decreases rapidly for stars of spectral type M5 or later, with the values of $L_{\rm X}$ measured for CN Leo more than an order of magnitude lower than those found for the sample of Robrade & Schmitt (2005). Thus there are only a few late-type M dwarfs for which X-ray spectra of reasonable quality are available. The binary UV Cet (M5.5) has been spatially resolved by *Chandra* (Audard et al. 2003a) with $\log L_{\rm X} \sim 27.0$ for both components and a temperature of 3–6 MK. UV Cet was also searched for Fe XIII by Fuhrmeister et al. (2004), but due to its high rotational velocity only indirect evidence of the line could be found; therefore the question of whether UV Cet shows the forbidden Fe XIII line is still not settled at the moment. Another case is Proxima Centauri, where also no definitive statement could be made concerning Fe XIII line emission. A 65 ks observation with *XMM* showed quasi-quiescent emission at a level of $\log L_{\rm X} \sim 26.8$, as well as a huge long-duration flare with a peak luminosity of $\log L_{\rm X} = 28.5$ (Güdel et al. 2002a, 2004).

The lack of good X-ray data for very late-type M dwarfs and the uniqueness of CN Leo with respect to the persistent emission of the Fe XIII line suggests strictly simultaneous X-ray

---

[*] Based on observations collected at the European Southern Observatory, Paranal, Chile, 076.D-0024(A) and on observations obtained with *XMM-Newton*, an ESA science mission with instruments and contributions directly funded by ESA Member States and NASA.

Table 1. Observation log for CN Leo.

Instrument	Mode	Observation Time	Duration [s]
UVES	Dichroic 1 (346 / 564 nm)	2004-05-19T22:45–22:48	1 × 260 / 1 × 260
MOS 1&2	Full Frame / Medium filter	2004-05-19T20:46–20T03:13	22 500
PN	Large Window / Medium filter	2004-05-19T22:43–20T03:08	15 900
RGS 1&2		2004-05-19T20:46–20T03:16	20 600
UVES	Dichroic 1 (346 / 564 nm)	2005-12-11T06:46–09:01	8 × 975 / 16 × 450
MOS 1&2	Full Frame / Medium filter	2005-12-11T05:38–10:46	18 500
PN	Large Window / Medium filter	2005-12-11T06:07–10:41	16 500
RGS 1&2		2005-12-11T05:37–10:50	18 700
UVES	Dichroic 1 (346 / 564 nm)	2005-12-13T08:00–09:06	4 × 975 / 8 × 450
MOS 1&2	Full Frame / Medium filter	2005-12-13T03:59–08:59	18 000
PN	Large Window / Medium filter	2005-12-13T04:28–08:54	15 600
RGS 1&2		2005-12-13T03:59–09:02	17 700

observations of CN Leo with a modern X-ray telescope such as *XMM-Newton* to determine coronal temperatures and densities and high-spectral resolution optical/UV observations, allowing studies of the chromospheric emission and the coronal Fe XIII line from the ground. In this paper we report on a multiwavelength campaign designed to cover the coronal and chromospheric properties of CN Leo by simultaneous observations in the optical and in the X-ray regime. In the subsequent sections we first describe our observations obtained with *XMM-Newton* and VLT/UVES in Sect. 2. In Sect. 3 we analyse the timing behaviour of CN Leo during the observations. The derived X-ray properties are presented in Sect. 4, while the analysis of the behaviour of the chromospheric lines is found in Sect. 5. A discussion and our conclusions are found in Sects. 6 and 7.

2. Observations and data analysis

The multi-wavelength observations reported in this paper were obtained strictly simultaneously with *XMM-Newton* and ESO's Kueyen telescope equipped with the Ultraviolet-Visual Echelle Spectrograph (UVES) on one night in May 2004 (19th/20th), and on two nights in December 2005 (11th/12th and 13th/14th); an overview of the observational parameters can be found in Table 1. Similar observations with, however, somewhat different instrumental setups both in the optical and in the X-ray band were performed in May 2006 and will be discussed in forthcoming papers.

UVES is an cross-dispersed echelle spectrograph mounted on the Nasmyth B focus of the Kueyen telescope (UT2). It can be operated in different wavelength intervals in the range from about 3000 to 11 000 Å. The light is dispersed onto two arms, each of which can be used either alone or in parallel using a dichroic beam splitter. Thus a large part of the optical wavelength range can be observed in a single exposure with an average resolution of ~40 000. The blue spectrum is recorded with a single CCD detector, while the red arm is covered by a mosaic of two CCD chips, leading to a small gap in the red spectrum. While the chips for the blue arm and the bluer part of the red arm are identical (type EEV CCD-44), the CCD chip used for the redder part of the red arm is of type MIT/LL CCD-20, leading to reduced fringing[1]. In our specific setup used for the CN Leo observations presented here, the spectral coverage was between 3200 Å to 3860 Å in the blue arm and 4590 Å to 6620 Å in the red arm with a small gap from 5640 Å to 5660 Å due to the CCD mosaic.

All of the optical data analysed here were taken in service mode. Unfortunately, because of poor weather at Paranal, the optical observations for the 2004 campaign were almost totally lost. Only one red arm spectrum could be obtained at 22:45 UT with an exposure time of 260 s. The signal in the corresponding exposure in the blue arm is too low, leaving only the red arm spectrum with useful data. We used the UVES pipeline products that provide an absolute flux calibrated spectrum for this single exposure. The optical observations in December 2005 yielded a total of 36 spectra. For this run we used exposure times of 975 s and 450 s for the blue and the red parts of the spectrum, respectively. The optical spectra from this run were reduced using the IDL-based `REDUCE` reduction package (Piskunov & Valenti 2002). The wavelength calibration was carried out using Thorium-Argon spectra and resulted in an accuracy of ~0.03 Å in the blue arm and ~0.05 Å in the red arm. Absolute flux calibration was carried out using the UVES master response curve and extinction files provided by ESO. In addition to the high-resolution spectra, there are photometric data with a time resolution of approx. 1 s from the UVES exposuremeter, which are, however, not flux-calibrated.

On board *XMM-Newton* there are three co-aligned X-ray telescopes, accompanied by the OM (Optical Monitor), an optical/UV telescope. Each of the three X-ray telescopes is equipped with one of the EPIC (European Photon Imaging Camera) instruments, CCD detectors providing medium-resolution imaging spectroscopy with $E/\Delta E \approx$ 20–50 and timing analysis with a time resolution at the subsecond level. Two of the EPIC instruments are the identical MOS1 and MOS2 detectors operating in the energy range of 0.2–12.0 keV. The third EPIC instrument, the PN detector, covers the energy range of 0.2–15.0 keV with higher sensitivity, while the MOS detectors provide a better angular and spectral resolution; several filters and operating modes are available for these instruments. The X-ray telescopes with the MOS detectors also are equipped with reflective gratings and their corresponding CCD detectors. These Reflection Grating Spectrometers (RGS1 and RGS2) provide high-resolution spectroscopy in the energy range of 0.35–2.5 keV (5–38 Å) with $E/\Delta E$ of 200 to 800 and a spectral resolution of ≈0.06 Å *FWHM* so that the individual X-ray emission lines can be resolved. All instruments can be operated simultaneously and provide multiple measurements of the same target[2].

---

[1] A detailed description of the UVES spectrograph is available under `http://www.eso.org/instruments/uves/doc/`

[2] More details on the instruments onboard *XMM-Newton* can be found in the *XMM-Newton* Users' Handbook, available at `http://xmm.vilspa.esa.es/external/xmm_user_support/documentation/uhb/index.html`

Our *XMM-Newton* X-ray observations have durations of 20 ks (ObsID 0200530201) in May 2004 and 18 ks each (ObsIDs 0200530301 and 0200530401) in December 2005, and thus fully cover the time spanned by the optical observations (see also Figs. 1 and 2). The PN and MOS detectors were operated in full frame and large window mode with the medium filter. All X-ray data were reduced with the *XMM-Newton* Science Analysis System (SAS) software, version 7.0. EPIC lightcurves and spectra were obtained using standard filtering criteria. Spectral analysis was carried out with XSPEC V12.2 (Arnaud 1996), making use of two- and three-temperature component models with coupled abundances for each component. The plasma models assume a collisionally-ionised, low-density optically-thin plasma as calculated with the APEC code (Smith et al. 2001). Abundances are calculated relative to the solar photospheric values from Anders & Grevesse (1989). Due to the proximity of CN Leo, interstellar absorption is negligible for the optical as well as for the X-ray data. Additionally we made use of the CORA program (Ness & Wichmann 2002) to measure individual line fluxes in the RGS and UVES spectra.

3. Spectra and timing behaviour

3.1. X-ray and optical light curves

In Fig. 1 we plot the X-ray light curve (taken with EPIC-PN) of our May 2004 run, while the X-ray light curves (taken with EPIC-PN) for the two observation runs from December 2005 are shown in Fig. 2, also indicating the time overlap between the UVES and *XMM-Newton* data sets; the X-ray light curves were binned in 100 s bins. The individual blue-arm exposures are also indicated and numbered for easy reference. The exact start times for each blue exposure are listed in Table 4. Two red exposures cover one blue exposure and will be referenced with numbers using step size 0.5.

In the X-ray data from December 11th 2005 (cf., Fig. 2, left panel), a shallow slope is apparent in the light curve, which we tentatively interpret as part of the decay phase of a very long-duration flare, the onset of which is not covered by our observations. The enhanced level of activity during this state is shown by the X-ray fluxes and the chromospheric emission lines, which will be discussed later.

There is also relatively weak X-ray flickering with two small flares at about 07:30 and 10:00 UT and a larger one at about 09:00 UT with an increase in count rate of about a factor of two. The flare at 07:30 UT, lasting about three minutes, is covered by UVES and also seen in the photometric data. In the blue arm it is covered in spectrum number 3 and in the red arm in spectrum number 3.5. The flare lasted for about three minutes and there was no detectable delay between the optical and the X-ray data at variance with a possible Neupert effect.

The X-ray light curve from December 13th (cf., Fig. 2, right panel) shows the onset of another strong flare at its end; unfortunately the flare peak is not covered by our data. It is preceded by a short duration flare, which is also found in the optical photometer data; the corresponding UVES spectrum is spectrum number 11 (for the blue and the red arms). The short duration flare lasts about four minutes. With a binning of 10 s for the X-ray and optical data, we found that the optical peak precedes the X-ray peak by about one minute. Such delays are expected if the Neupert effect is at work, however, count statistics prevent us from verifying that the time derivative of the soft X-ray light curve does indeed approximate the shape of the optical light curve. Note that the increasing optical flux at the end of both observation runs is partly due to scattered sunlight indicating daybreak.

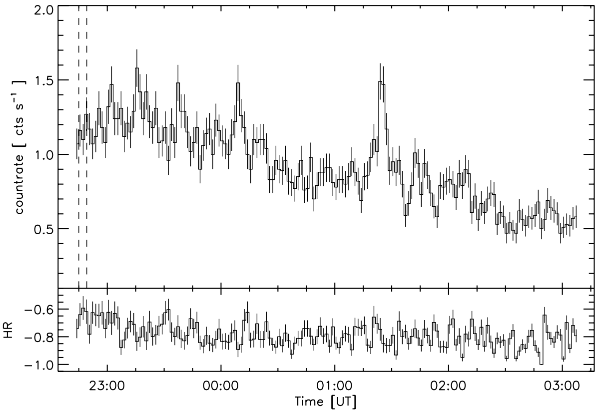

Fig. 1. X-ray light curve and hardness ratio of CN Leo from May 19/20, 2004 taken with the PN instrument with a bin size of 100 s. The vertical lines show the time interval of the simultaneous UVES observation.

The X-ray count rate for the May 2004 run is again somewhat lower than on December 13th. Besides some X-ray flickering, a small flare is observed at 1:30 UT. The X-ray light curve shows a similar but even stronger downward trend than the December 2005 data. Without the exposuremeter light curve and UVES spectra covering a longer period of time, especially the flare, we cannot make a statement about the simultaneous chromospheric activity.

In Figs. 1 and 2 we also show the time-dependent hardness ratios (HR); to derive HR, the source counts from the EPIC PN data are divided into "soft" and "hard" bands ranging from 0.15–1.0 keV (S) and 1.0 to 10.0 keV (H), respectively, and we define $HR = \frac{H-S}{H+S}$. The significance of the observed HR variations is difficult to assess; however, there seems to be a slight decrease from ≈−0.65 to −0.8 and thus a softening in the first quarter of the May 2004 observations. No clear indications of spectral changes related to the small flare are observed. Apart from a clear hardening to ≈−0.5 during the large flare at 9:00 UT, the hardness ratio of the December 11th 2005 observation seems to be more or less constant at a level of ≈−0.65 without a significant increase related to the two smaller flares, since other variations apparently unrelated to variations in the lightcurve are within the same order of magnitude. On December 13th, the hardness ratio slowly increases from ≈−0.75 to −0.6 at approximately 6:30 UT, then decreases back to −0.75, with a new increase obviously coupled to the two flares towards the end of the observation.

3.2. X-ray spectra and fluxes

We analysed the overall X-ray flux using the PN spectra from the individual runs in May 2004 and December 2005. The X-ray flux levels change significantly for the three exposures, as can be seen in Fig. 3; the X-ray flux was determined using the XSPEC best-fit spectral models (see Sect. 4) in the energy range 0.2 to 2.0 keV. Specifically, the 2004 EPIC PN exposure results in an X-ray flux of 2.1×10^{-12} erg cm^{-2} s^{-1} ($L_X = 1.4 \times 10^{27}$ erg s^{-1}), the December 13th exposure gives 4.3×10^{-12} erg cm^{-2} s^{-1} ($L_X = 3.0 \times 10^{27}$ erg s^{-1}), and the data from December 11th give 7.6×10^{-12} erg cm^{-2} s^{-1} ($L_X = 5.2 \times 10^{27}$ erg s^{-1}). Since the X-ray luminosity of the 2004 run roughly agrees with the *ROSAT* X-ray luminosity,

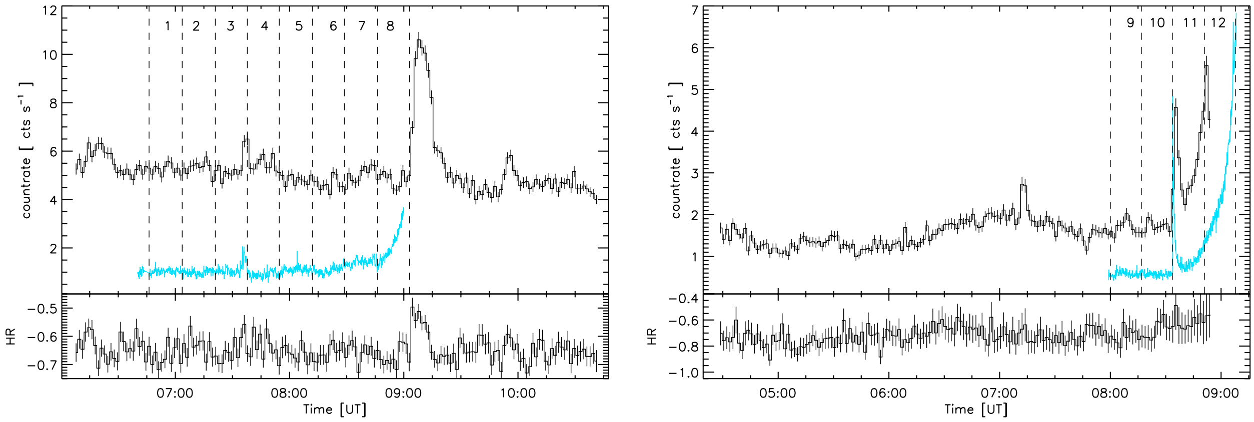

Fig. 2. Light curves in the optical and in X-rays plus an X-ray hardness ratio for 11 (*left*) and 13 (*right*) December 2005. The black curves denotes the *XMM* EPIC PN detector and the grey / light blue curves the blue UVES exposuremeter, which is scaled down in intensity by a factor of 30. The vertical dashed lines mark the beginning of the UVES exposures of the blue arm. Note that the steep rise of the exposuremeter data at the end of each UVES run is partly due to scattered light of the beginning dawn. The time bin size of the X-ray data is 100 s.

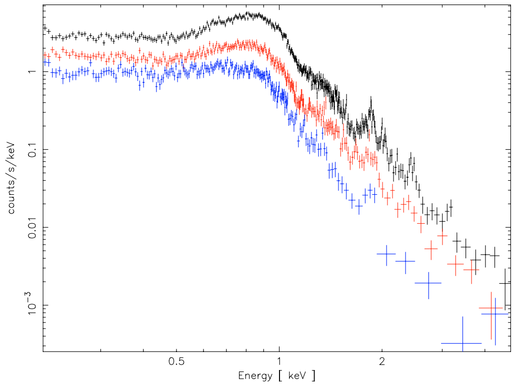

Fig. 3. PN spectra from the December 11th 2005 run (top/black), the December 13th run (middle/red), and the May 19th 2004 run (bottom/blue).

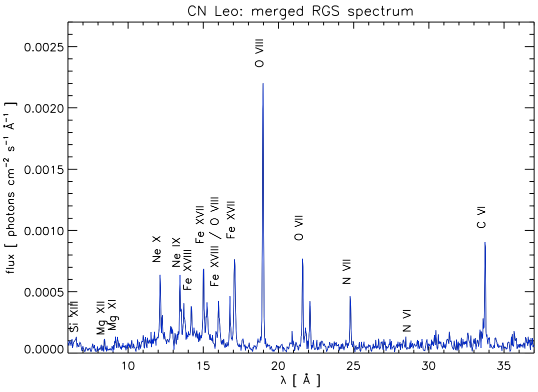

Fig. 4. RGS spectrum of CN Leo constructed from RGS 1 and 2 in 1st order with the SAS task `rgsfluxer` from all three observations. Prominent emission features are labelled.

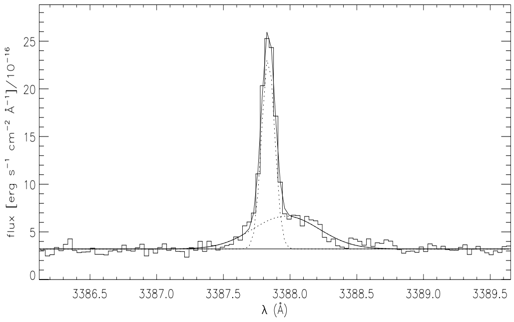

Fig. 5. The (broad) forbidden coronal Fe XIII line at 3388 Å blended with the narrow chromospheric Ti II line; this spectrum is averaged from spectra 1 to 6 to increase the signal-to-noise ratio.

CN Leo seems to have been in a quiescent state at that time, while both runs in December 2005 show higher X-ray flux, the second one even with the flaring period at the end of the observation excluded. The X-ray flux enhancement of the first night (December 11th) fits into the picture of CN Leo being in the decay phase of a long duration flare. Since even during the second night (December 13th) the X-ray flux is not as low as in May 2004, the star must have still (or again) been in a state of increased activity.

In Fig. 4 we show the co-added and fluxed RGS spectrum of CN Leo obtained from all three observations. It resembles the RGS spectra of other M-dwarfs (cf. Robrade & Schmitt 2005), with O VIII Ly α being the strongest line and other prominent lines originating from Ne IX and X, Fe XVII, O VII, and C VI. While the true source continuum is not very pronounced, a pseudo-continuum between ≈10–17 Å resulting from the broad wings of brighter Ne and Fe lines, plus additional weak and unresolved lines, is clearly visible.

3.3. The optical spectra

The typical spectral resolution of our UVES spectra is ~40 000. Unfortunately, the Hα line is saturated in our spectra; however, various members of the Balmer series are well-covered, i.e, Hβ in the red arm and H_9 and higher Balmer lines up to H_{24} in the blue arm. In contrast to earlier M dwarfs, CN Leo shows an almost pure chromospheric emission line spectrum in the blue without hardly any photospheric absorption lines. The quality of the optical spectra for the spectral range around the forbidden Fe XIII line can be assessed from Fig. 5. Since the signal-to-noise ratio in this very blue region is low, the spectrum around the Fe XIII line was averaged from spectra 1 to 6 from the first night, where little variation in the Fe XIII line is seen and variations in the blending Ti II line are also small.

Table 2. Absolute coronal abundances of CN Leo[1].

	C	N	O	Ne	Mg	Si	S	Fe
XSPEC	1.49 ± 0.24	1.28 ± 0.21	0.62 ± 0.08	1.20 ± 0.16	0.85 ± 0.17	0.78 ± 0.33	1.41 ± 0.27	0.59 ± 0.07
DEM method 1	1.27 ± 0.13	1.03 ± 0.13	0.66 ± 0.03	1.22 ± 0.11	0.92 ± 0.16	n.a.	n.a	0.56 ± 0.04
DEM method 2	1.18 ± 0.12	0.97 ± 0.12	0.63 ± 0.03	1.17 ± 0.11	0.85 ± 0.15	n.a.	n.a	0.55 ± 0.04

[1] Abundances are derived from the RGS and EPIC data as fitted with a three component temperature model as described in Sect. 4.1. Methods 1 and 2 use a differential emission measure method as described in Sect. 4.2. The given errors are the statistical 1σ standard deviations.

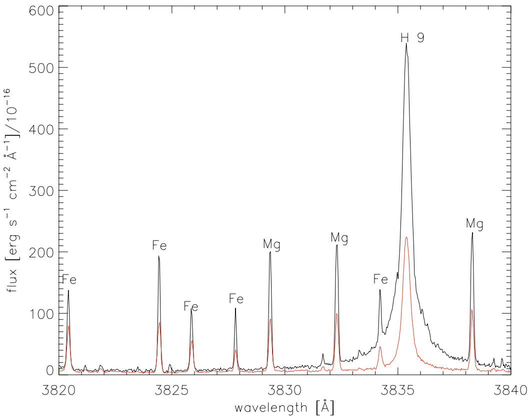

Fig. 6. Spectral range around the H_9 line; various metal lines of Fe I and Mg I are indicated. The black spectrum is number 12 taken during the flare, the red/grey spectrum is number 1 from the December 11th 2005 run.

A much higher signal-to-noise ratio is obtained at the red end of the blue spectral arm, where most of the lines used for the chromospheric analysis are located. The spectral wavelength range around the H_9 line is shown in Fig. 6 for the quiescent and the flaring case; note the broad wings of the H_9 line, especially during the flare. These broad wings can be fitted using a linear combination of two Gaussians. For $H\beta$, a fit with a Voigt function resulted in worse fits, while for H_9 a Voigt profile resulted in similar good fits compared with two Gaussian components. For consistency we decided to also fit H_9 and higher Balmer lines with two Gaussian profiles.

4. Coronal properties of CN Leo

4.1. Coronal abundances and temperatures

We determined plasma temperatures and abundances relative to solar values (Anders & Grevesse 1989) with an iterative procedure of global fits to the EPIC and RGS spectra with APEC plasma models. As a starting point, we used the merged RGS and EPIC spectra of all three observations. First we fitted a two-temperature component model to the RGS data to establish an initial set of abundances. Al, Ca, and Ni as elements with low first ionisation potentials (FIP) were coupled to Fe, and Ar as an element with a high first ionisation potential was coupled to Ne. Independent fits to these elements are not feasible due to the absence of pronounced lines in the RGS wavelength range. The thus determined abundances were fixed and used to determine the temperatures of a three-temperature component model fitting the EPIC data. The final abundances were then determined from a parallel fit to the RGS data with spectral bins below 6 Å excluded, and to the EPIC spectra restricted to the energy range from 1.2 to 5.0 keV (Table 2). Besides this global fit we also used two slightly different methods based on individual line fluxes from the RGS for comparison, as described in more detail in Sect. 4.2. The elemental abundances as determined from these line-based DEM methods are also listed in Table 2. An inspection of Table 2 shows that the abundances determined by the different methods are consistent within the errors, so we are confident that our abundances do not depend on the chosen analysis methods or models, while obviously the dependence on the atomic physics parameters remains.

While the Sun or stars with a low activity level often show an abundance pattern varying with the first ionisation potential (FIP), where the low FIP elements are enhanced in the corona, a reversed pattern – the inverse FIP effect – with depleted low-FIP elements and enhanced high-FIP elements is frequently found in stars of higher activity (e.g. Brinkman et al. 2001; Audard et al. 2003b). Although the abundance errors are relatively large, elements with low FIP like Mg, Fe, and Si seem to be less abundant in general than high FIP elements like C, O, N and Ne, indicating an inverse FIP effect.

We implicitly assume that our abundances do not change between the three observations and the changing states of activity, and therefore we fix the abundances at the values determined above. We then fitted temperatures and emission measures (EM) to the EPIC PN and MOS data in the energy range from 0.3–5.0 keV. We grouped the data for the first night into quiescent and flaring states, with the quiescent state representative of the state during the UVES exposures. The same procedure was applied to the second night, where the flaring state approximately corresponded to UVES exposures Nos. 11 and 12. The resulting fit parameters are listed in Table 3. We also binned the PN spectra into time intervals corresponding to the UVES exposures, where the exposures 9/10 and 11/12 had to be grouped to obtain higher signal. For these ten datasets, we fitted three overall temperature components with best-fit values of 0.26 keV, 0.64 keV, and 1.44 keV and with independent emission measures. The variation in the emission measures is shown in Fig. 9. Moreover we measured the broad band X-ray flux between 0.2 and 2.0 keV of these PN spectra as listed in Table 4.

Our spectral fits indicate two stable temperature components at about 2 MK (1 keV ≡ 11.6 MK) and a stronger one at about 7 MK. On December 11th and during the flare on December 13th 2005, there is also a strong high-temperature component at about 18 MK. During the flares, the emission measure of the 2 MK and 7 MK temperature components is enhanced, which is also the case for the first night compared to the second night and for the whole 2005 run compared to the 2004 run. This again shows the higher state of activity of CN Leo in December 2005 and especially on December 11th. The quiescent state of the observation from December 13th may also be fitted with two temperature components, and the corresponding fit parameters are also listed in Table 3. The three temperature component fit, however, provides a better fit result, while a three temperature component model does not further improve the fit for the May 2004 observation.

Table 3. Best fit temperatures and emission measures for two and three component APEC models using the PN and MOS data.

Date	State	kT_1 (keV)	EM_1 (10^{50} cm^{-3})	kT_2 (keV)	EM_2 (10^{50} cm^{-3})	kT_3 (keV)	EM_3 (10^{50} cm^{-3})	red. χ^2	d.o.f.
2004-05-19	quiescence	0.20 ± 0.01	0.21 ± 0.01	0.61 ± 0.01	0.23 ± 0.01			1.91	334
2005-12-11	quiescence	0.26 ± 0.01	0.79 ± 0.03	0.64 ± 0.01	1.49 ± 0.03	1.29 ± 0.02	0.64 ± 0.02	1.50	541
2005-12-11	flare	0.24 ± 0.02	0.90 ± 0.09	0.67 ± 0.01	1.94 ± 0.09	1.50 ± 0.09	1.04 ± 0.07	0.93	267
2005-12-13	quiescence	0.20 ± 0.01	0.30 ± 0.01	0.62 ± 0.01	0.48 ± 0.01			1.83	382
2005-12-13	quiescence	0.24 ± 0.01	0.33 ± 0.01	0.61 ± 0.01	0.40 ± 0.01	1.82 ± 0.20	0.09 ± 0.01	1.50	380
2005-12-13	flare	0.19 ± 0.01	0.40 ± 0.03	0.65 ± 0.01	0.97 ± 0.04	1.59 ± 0.07	0.83 ± 0.05	1.21	187

Table 4. Line-fit parameters of the Fe XIII and the Ti II line[1].

No.	date and UT	λ (Å)	Fe line flux (10^{-16} erg s^{-1} cm^{-2})	Half width (Å)	λ (Å)	Ti line flux (10^{-16} erg s^{-1} cm^{-2})	half width (Å)	X-ray flux (10^{-12} erg s^{-1} cm^{-2})
1	2005-12-11T06:46	3387.95 ± 0.26	2.5 ± 0.6	0.29	3387.82 ± 0.04	3.2 ± 0.4	0.05	7.29
2	2005-12-11T07:03	3387.94 ± 0.20	2.5 ± 0.5	0.23 ± 0.01	3387.81 ± 0.04	3.0 ± 0.4	0.05	7.42
3	2005-12-11T07:20	3388.05 ± 0.31	2.0 ± 0.5	0.28	3387.82 ± 0.05	2.9 ± 0.4	0.06	7.01
4	2005-12-11T07:37	3387.93 ± 0.25	1.5 ± 0.5	0.26 ± 0.03	3387.82 ± 0.04	2.2 ± 0.4	0.05	7.81
5	2005-12-11T07:54	3387.94 ± 0.21	2.5 ± 0.5	0.23 ± 0.01	3387.82 ± 0.04	2.1 ± 0.4	0.05	6.83
6	2005-12-11T08:11	3387.96 ± 0.21	2.2 ± 0.5	0.23 ± 0.01	3387.82 ± 0.03	2.2 ± 0.4	0.04	6.43
7	2005-12-11T08:29	3387.98 ± 0.24	2.4 ± 0.6	0.25 ± 0.02	3387.82 ± 0.04	3.4 ± 0.4	0.05	6.84
8	2005-12-11T08:46	3387.95 ± 0.22	2.5 ± 0.6	0.24 ± 0.02	3387.83 ± 0.03	3.5 ± 0.4	0.04	6.77
9	2005-12-13T07:59	3387.98 ± 0.23	1.3 ± 0.4	0.21	3387.81 ± 0.05	1.1 ± 0.3	0.04	
10	2005-12-13T08:16	3388.01 ± 0.29	1.7 ± 0.4	0.29	3387.83 ± 0.07	0.6 ± 0.2	0.04	
11	2005-12-13T08:33	3387.99 ± 0.45	1.5 ± 0.7	0.29	3387.82 ± 0.03	2.8 ± 0.4	0.04	
12	2005-12-13T08:50	3387.88 ± 0.30	1.7 ± 0.7	0.25 ± 0.03	3387.81 ± 0.03	6.0 ± 0.5	0.04	

[1] Both lines have been fitted using Gaussians with the central wavelength, amplitude, and halfwidth as free parameters. The broad band X-ray flux is given between 0.2 and 2.0 keV.

4.2. Differential emission measure

In addition to the global fits we used other approaches to assess the coronal abundances of CN Leo. These methods make use of individual line fluxes measured from the *XMM-Newton* RGS. In order to achieve better signal-to-noise, we co-added the RGS spectra of all three observations with the SAS task `rgscombine`, here also assuming that the abundances did not change.

We reconstructed the shape of the differential emission measure (*DEM*) from abundance-independent ratios of the H-like Lyα and the He-like resonance lines from N, O, Ne, and Mg and from additional ratios of Fe XVII and Fe XVIII lines. The high-temperature slope of the *DEM* was also constrained by the ratio of continuum flux measurements at wavelengths around 7.5 Å and 20 Å, where the spectrum is essentially free of any clear lines; the latter continuum interval is also used for normalisation. As a result of the merging of the three RGS datasets, the determined *DEM* constitutes an average of these observations with their different states of activity and quiescent and flaring periods.

We used two slightly different approaches to model the *DEM*. First we fit $\log DEM$ as a function of $\log T$ with polynomials of different orders with no further constraints (method 1), while in a second approach we model the linear *DEM* again with polynomials and as a function of $\log T$. In this second approach, the fit polynomial is then forced to have two zeros at variable temperatures, thereby defining the boundaries of the coronal emission measure distribution (method 2). The two approaches will be described in detail in Liefke & Schmitt (2007). Both methods give acceptable fit results already with 3rd (method 1) and 4th (method 2) order polynomials, with values of reduced χ^2 of 1.29 and 1.14, respectively. The resulting differential emission measure distributions are shown in Fig. 7, and they peak at temperatures of $\log T \approx 6.4$ ($T = 2.5$ MK). When introducing higher-order polynomials (orders 5 and 6), the *DEM* develops a two-peaked structure with maxima at $\log T \approx 6.3$ and 6.8–6.9, probably associated with the low-temperature component of the quiescent phases and the hotter component related to the flares and the higher level of activity during the whole December 11th observation. Since we cannot be sure about the reality of these structures in the *DEM*, we prefer the "simpler" *DEMs* with fewer free parameters according to Occam's razor.

With the differential emission measure from both methods, we then determined abundances as shown in Table 2 by forcing the *DEM*, abundance and line emissivities to reproduce the measured line fluxes according to $f = \frac{Ab(X)}{4\pi d^2}\int G(T)DEM(T)\,\mathrm{d}T$, with the line flux f, the line contribution function $G(T)$, and the abundance $Ab(X)$ of element X generating the line. Note that the quoted errors result exclusively from count statistics of the flux measurements and assume (admittedly somewhat unrealistically) that the reconstructed *DEM* is free of errors. Especially the errors do not include the uncertainties of 12% on the continuum flux (originating from count statistics) propagating into the overall normalisation of the *DEM* and thus also into the absolute level of the abundances. Compared to the normalisation uncertainties due to low signal-to-noise of the continuum flux measurements, Liefke & Schmitt (2007) assess that uncertainties in the shape of the *DEM* have a smaller influence on the abundances, typically less than 5%.

To demonstrate the goodness of fit for our *DEM* fitting techniques, we used the determined *DEM*s and corresponding deduced sets of abundances to calculate synthetic spectra with CHIANTI (Landi et al. 2006). These synthetic spectra are in very good agreement with the RGS spectra, and the EPIC spectra are also reproduced quite well. Figure 8 shows the fit of

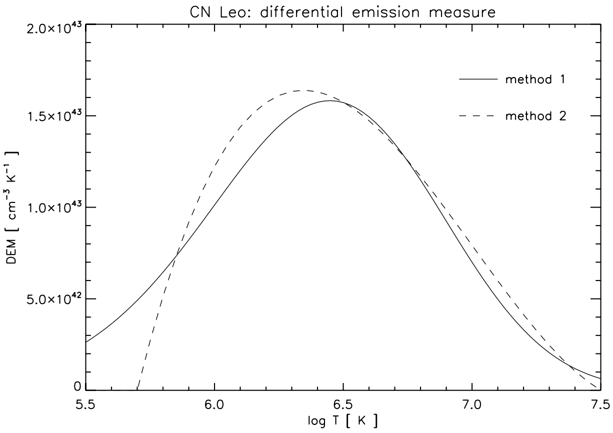

Fig. 7. Differential emission measure for CN Leo as determined by a 3rd-order polynomial fit (method 1) and a 4th-order polynomial fit (method 2) of line ratios from the combined RGS observations. Note that the shape of the *DEM* at temperatures $\log T < 6$ cannot be determined from the available line ratios.

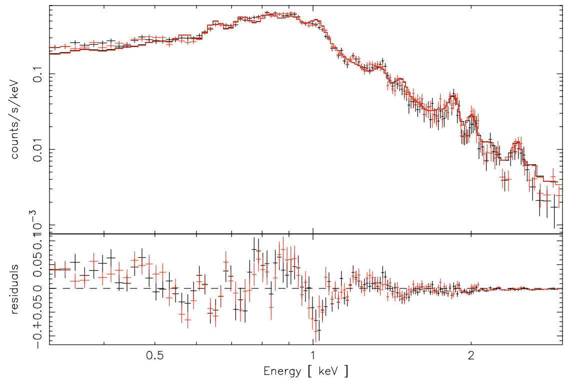

Fig. 8. Comparison of a synthetic spectrum based on the *DEM* model and abundances from method 2 to the MOS1 (black) and MOS2 (red) spectra. The agreement is remarkably good, considering that the model has been determined independently from the EPIC data.

the model spectrum determined from the *DEM* and abundances from method 2 to the combined MOS spectra of the three observations. Some slight systematic deviations related to individual emission features seem to be present, e.g. near 1 keV, indicating an overprediction of Ne X, while the discrepancies at low energies are probably due to RGS-EPIC cross-calibration problems.

4.3. Coronal densities

We estimated coronal plasma densities using the density-sensitive ratio of the forbidden and intercombination lines of the O VII triplet from the three *XMM* observations. This method is described in Gabriel & Jordan (1969) and was extensively used by Ness et al. (2002, 2003). The measured f/i ratios are 2.63 ± 1.28 in May 2004, 1.60 ± 0.46 (2.03 ± 0.67 with the flare excluded) for the December 11th 2005 observation, and 1.91 ± 0.74 (2.58 ± 1.28 with the flare excluded) for the December 13th 2005 observation run. Given the large errors of these line ratios (caused by the weak intercombination line), it is difficult to claim significant changes during the individual data runs.

For the conversion of the measured f/i ratios to densities, we used the relation $f/i = R_0/(1 + n_e/N_c)$ with the low-density limit R_0 and the critical density N_c where we adopted the values from Pradhan & Shull (1981) of 3.95 and 3.1×10^{10} cm^{-3}, respectively. The average O VII f/i-ratio of 1.72 ± 0.35 is well below the low-density limit and corresponds to $n_e = 4.0^{+1.9}_{-1.2} \times 10^{10}$ cm^{-3}. Concerning the individual observations, we find electron densities of $n_e = 4.5^{+3.1}_{-1.7} \times 10^{10}$ cm^{-3} for December 11th 2005 and $n_e = 3.3^{+4.1}_{-1.8} \times 10^{10}$ cm^{-3} for December 13th using the whole data sets. When excluding the flaring periods, we find a slightly lower density of $n_e = 2.9^{+3.0}_{-1.5} \times 10^{10}$ cm^{-3} for the first night. During the second night, the f/i ratio yields $n_e = 1.6^{+4.7}_{-1.6} \times 10^{10}$ cm^{-3}, consistent with the low-density limit. The same applies to the complete May 2004 observation. Thus the data suggest an increase in plasma density during the flares and for the first night. However, if the uncertainties are accounted for all the deduced densities are consistent within the errors. The corresponding f/i ratios of the Ne IX triplet always point to the low-density limit.

4.4. The forbidden coronal Fe XIII line

In addition to the X-ray data obtained with *XMM-Newton*, the coronal properties of CN Leo can be assessed using the forbidden coronal Fe XIII line at 3388 Å. As is well known, this line is blended with a Ti II chromospheric line (see Fig. 5), but can be "deblended" with a suitable fit procedure. The results from a simultaneous fit of the two lines with CORA are presented in Table 4. The central reference wavelengths of both lines are provided through NIST (`http://physics.nist.gov/PhysRefData/ASD/index.html`) as 3387.84 Å for the Ti II line and 3388.1 Å for the Fe XIII line, which agrees with the central wavelength found in the fit for both lines. While the amplitude of the Ti II line reacts to the flare onsets in spectrum number 7/8 and 11/12, the Fe XIII line stays more or less constant for both nights albeit at different flux levels. The mean Fe XIII flux ratio between the first and the second night is 1.5 ± 0.3, in agreement with the X-ray flux ratio of 2.2 ± 0.4 measured from the RGS data of O VII resonance lines that have about the same peak formation temperature 1.6 and 2 MK for Fe XIII and O VII respectively, while the hotter 5 MK X-ray Fe XVII lines show a flux ratio of 3.5 to 4. Exclusion of flare time intervals leads to ratios of 2 to 3 depending on the Fe XVII lines used. Also the Fe XIII flux ratio is in agreement with the ratio of 1.8 for the EM of the cool 2 MK component.

The measured broad-band X-ray flux of the PN spectra corresponding to the UVES exposure time intervals also reflects the general behaviour of the forbidden Fe XIII line (see Table 4), with the flux being lower on December 13th than on December 11th. However, the X-ray flux of course reacts strongly to the flare occurring during exposures Nos. 11 and 12. The Fe XIII line strength should be traced better by the emission measure of the low temperature component that approximately corresponds to the formation temperature of Fe XIII. Figure 9 shows the two flux different levels of the Fe XIII line on the two days. The low temperature component also has slightly lower emission measures on the second day, but it is difficult to confirm this trend with only two data points (and one of them affected by flares). On the contrary, the two hotter components are lower by factors greater than 2 during exposures Nos. 9 and 10 compared to the first night, increasing again (especially the very hot component) during the flare.

In order to assess the absolute flux variations, we computed the expected flux of the Fe XIII line from its emissivity as incorporated in the CHIANTI database, the differential emission

Table 5. Measured fluxes for the Balmer lines and other chromospheric emission lines in 10^{-16} erg s^{-1} cm^{-2} (narrow and broad components).

No.	$H\beta$	H_9	H_{10}	H_{11}	H_{12}	H_{13}	H_{14}	H_{15}	Na D	Na D	He D_3	Ti II
									5889 Å	5895 Å		3372 Å
1	2193	132 (–1.22)	108 (–1.31)	88 (–1.40)	59 (–1.57)	34 (–1.81)	24 (–1.96)	16 (–2.09)	274	194	161	3.7
2	2082	124 (–1.23)	99 (–1.32)	83 (–1.40)	50 (–1.62)	31 (–1.83)	19 (–2.04)	13 (–2.14)	273	193	154	3.5
3	2052	129 (–1.20)	101 (–1.31)	80 (–1.41)	58 (–1.55)	32 (–1.81)	22 (–1.97)	13 (–2.12)	265	186	156	3.4
4	1856	103 (–1.26)	82 (–1.35)	66 (–1.45)	47 (–1.60)	27 (–1.84)	19 (–1.99)	13 (–2.11)	270	195	143	2.6
5	2032	117 (–1.24)	92 (–1.34)	77 (–1.42)	53 (–1.58)	31 (–1.82)	21 (–1.99)	14 (–2.11)	282	201	152	2.4
6	1946	121 (–1.21)	86 (–1.35)	71 (–1.44)	45 (–1.64)	26 (–1.87)	18 (–2.03)	11 (–2.18)	254	178	147	2.1
7	2605	144 (–1.26)	112 (–1.37)	90 (–1.46)	56 (–1.67)	33 (–1.90)	22 (–2.07)	14 (–2.20)	329	235	196	4.0
8	2261	138 (–1.21)	97 (–1.37)	74 (–1.49)	61 (–1.57)	35 (–1.81)	24 (–1.97)	17 (–2.08)	307	267	177	4.0
9	1252	74 (–1.23)	57 (–1.34)	47 (–1.43)	34 (–1.57)	19 (–1.82)	12 (–2.02)	9 (–2.09)	186	129	99	1.4
10	1130	67 (–1.23)	47 (–1.38)	31 (–1.56)	29 (–1.59)	16 (–1.85)	10 (–2.05)	8 (–2.13)	169	113	79	1.1
11	2228	221 (–1.00)	147 (–1.18)	113 (–1.29)	81 (–1.44)	44 (–1.70)	24 (–1.96)	16 (–2.05)	230	163	215	3.4
12	3769	480 (–0.89)	302 (–1.10)	220 (–1.23)	179 (–1.32)	97 (–1.59)	65 (–1.76)	41 (–1.89)	352	272	407	7.0

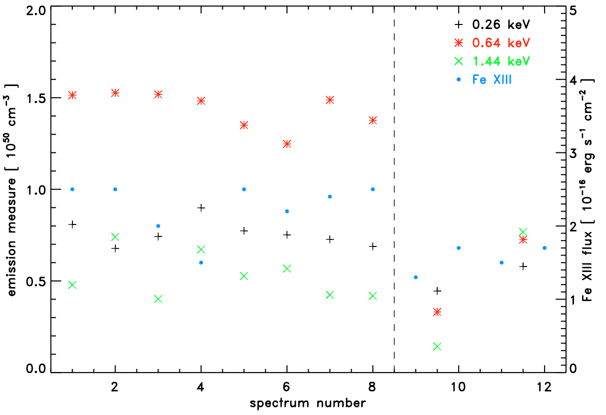

Fig. 9. Variations in the line flux of the Fe XIII line and the corresponding emission measures of the cool, intermediate, and hot temperature component of the X-ray spectra. The vertical dashed line divides the two nights of the December 2005 observations. Note that flux variations within individual nights are not statistically significant.

measures reconstructed from the RGS data (see Sect. 4.2) and the corresponding iron abundances (see Table 2), resulting in predictions of 6.3×10^{-16} erg s^{-1} cm^{-2} and 6.9×10^{-16} erg s^{-1} cm^{-2} with method 1 and 2, respectively. These values must be compared to a mean of $(2.5 \pm 0.6) \times 10^{-16}$ erg s^{-1} cm^{-2}, measured directly from our UVES spectra. Various sources of error contribute to the overall uncertainties of both values, and it is difficult to assess which one dominates here. The main uncertainties of the X-ray prediction arise from the underlying atomic physics of the iron lines: On the one hand, there are systematic outliers among the strong Fe XVII and Fe XVIII lines defining the mean iron abundance; we found discrepancies of up to 25% from the error-weighted mean for CN Leo, as well as for other stars. On the other hand, systematic errors in the theoretical line emissivity of the Fe XIII line itself are difficult to evaluate. Uncertainties in the shape of the reconstructed *DEM* should only contribute to a lesser extent to the overall error estimate as mentioned above; and the uncertainties in the overall normalisation of the *DEM* and the corresponding global abundance level cancel out. Regarding the optical flux measurements, the errors of ≈20% are purely statistical, and it is a little hard to assess systematic errors like the quality of the absolute flux calibration of our optical spectra. Nevertheless, we consider the agreement between the simultaneously measured, but independently derived, flux values as satisfactory.

5. Chromospheric and transition region properties of CN Leo

In the following we address the chromosphere and transition region of CN Leo. We specifically considered the He I D_3 line, the Na I D line, four Ti II lines in the wavelength range 3370 to 3390 Å, and the Balmer lines ($H\beta$, H_9 to H_{15}), together with several blending metal lines. We refrained from fitting the higher Balmer lines up to H_{24}, since the background determination is difficult for these higher-order lines, and some of them are severely blended with metal lines. All line fluxes were fitted with CORA, the line fluxes of the Balmer lines, and the Balmer decrements with respect to the $H\beta$ line (given in parenthesis) are listed in Table 5. The flux in the $H\beta$ line, in the Na D lines, and in the He D_3 line is the mean from the two red spectra taken during each blue exposure. We estimate the measurement errors especially for the higher lines to be about 10 percent mainly due to uncertainties in the background determination.

The downward trend in the X-ray light curve on December 11th is also reflected in the line fluxes of various chromospheric lines, e.g. in the four Ti II lines in the vicinity of the Fe XIII line, in the He D_3 line, and somewhat less clearly in the Balmer lines as well as in metal lines originating in the mid-to-lower chromosphere. Interestingly, this trend is not found in the line fluxes of the Na I D lines, but a stronger flux is visible in the first night than in the second night as for all other chromospheric emission lines as well as in X-rays. Also the ratio of the line fluxes for many chromospheric lines (for example the Mg I line at 3832.28 Å and the Fe I line at 3824.42 Å, but also the four Ti II lines) compared to the Balmer lines (here H_9) is higher for the first night. This may indicate that these lines evolve more slowly than the Balmer lines. Due to the coarse time resolution of the UVES spectra, the small flare at 07:30 UT is not found in a line flux increase for any measured chromospheric line, but it can be noticed as a broadening of the base of all the Balmer lines and an increase of the flux in the broad component compared to the narrow component.

A flare-like feature preceding the X-ray flare starting at 09:03 UT was also found in the chromospheric lines, starting at 08:20 UT and ending at 08:45 UT. This feature was indicated by a line flux increase in all chromospheric emission lines and a line broadening of the Balmer lines. Both started to decrease again in the blue spectrum number 8 and in the red spectra number 8.0 and 8.5, respectively. There was no corresponding feature either in the X-ray light curve or in the UVES photometer data. This brightening and broadening of the chromospheric lines preceded the X-ray flare peak by about 20 min. This is slightly more than

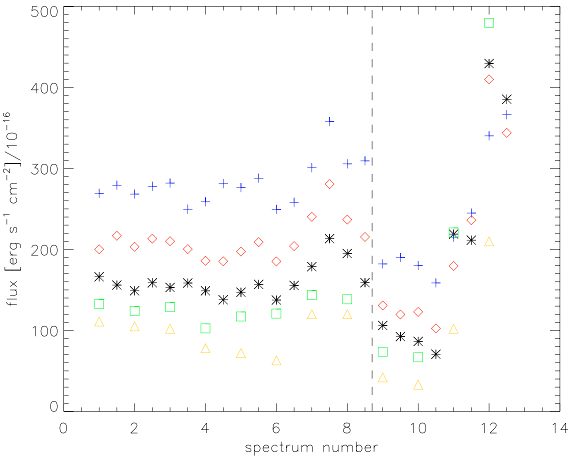

Fig. 10. Line fluxes of various chromospheric emission lines. The black asterisks denote the He I D$_3$ line, the red diamonds the Hβ line scaled down by a factor of 10, the blue crosses the Na I D line at 5889 Å, the green squares the H$_9$ line, and the yellow triangles the Ti II line at 3372 Å scaled up by a factor of 30. The vertical dashed line marks the onset of the second night.

the 10 min offset Mitra-Kraev et al. (2005) found between UV and X-ray lightcurves for active M dwarfs.

On December 13th, the chromospheric lines reacted strongly to both the short duration flare and to the onset of the large flare. In this case there was no time lag between the X-ray data and the chromospheric lines. With the higher time resolution of the red spectra, a decline in the line broadening for Hβ after the short duration flare could be noticed before an extreme broadening set in. The variation of the line fluxes for various chromospheric emission lines for both nights are shown in Fig. 10. Broad components in the Balmer and other chromospheric and transition region lines were found for several M dwarfs, either as symmetric or asymmetric (blue or red wing enhanced) profiles. Asymmetric line wings are usually interpreted as due to downward or upward mass motions (see Fuhrmeister et al. 2005a; Crespo-Chacón et al. 2006, and references therein). Symmetric broadenings, which can be described by two Gaussian line components, have been described e.g. by Hawley et al. (2003). The symmetric broadening observed here can be due to either high turbulent velocities or Stark broadening caused by high electron densities. Since the broad component is also found outside the detected flares, Stark broadening seems to be an unlikely explanation, since the required electron densities are expected to be reached only during flares. On the other hand mass motions outside the obvious flares may be caused by microflares, therefore we favour an interpretation via turbulent mass motions.

In addition to the chromospheric emission lines, we find two He II lines at 3203.1 Å and 4685.7 Å originating in the transition region during the flare on December 13th. According to CHIANTI, the line at 3203.1 Å consists of 10 components from which only the 6 components between 3203.12 Å and 3203.19 Å are seen. The line at 4685.7 Å shows a double peak in the data, out of which we associate two CHIANTI components out of four to the first peak (4685.38 Å and 4685.41 Å) and all nine CHIANTI components (from 4685.71 Å to 4685.93 Å) to the second peak. Two additional components at 4685.54 Å and 4685.58 Å do not seem to be present in the data. We fitted the 3203.1 Å line using a single Gaussian profile and the 4685.7 Å using two Gaussian profiles. For the red line we also applied a non-constant background since there are many molecular lines present in the considered wavelength range, but used the first spectrum of the series as a background spectrum, assuming that there is no He II emission present outside the flare. Applying this procedure, we fitted the 4685 Å He II line in the spectra 11, 11.5, 12, and 12.5. The amplitude of the line in spectrum 11.5 is very low, therefore we excluded the fit from further analysis. Also we excluded the fit of the 12.5 spectrum because the first component of the 4685.7 Å could not be fitted well in this spectrum. The fit for spectrum 12 is shown in Fig. 11. The line fluxes, as well as their ratios, can be found in Table 6. Using the line flux ratios and CHIANTI, we also obtained rough estimates of the chromospheric electron density and temperature. We also verified that no consistent result can be found, if the missing components of the two lines are included, assuming that the same components are seen in both spectra. For spectrum 11 (which includes the short duration flare) we find a temperature of about $\log T = 4.7$ and an electron density of about $\log n_e \gtrsim 10.0$ cm^{-3} and for spectrum 12 $\log T \approx 5.0$ and $\log n_e \approx 10.0$ cm^{-3}. The temperatures correspond approximately to the peak formation temperature of He II of $\log T = 4.7$.

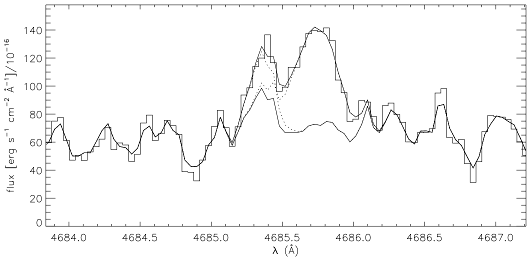

Fig. 11. Fit of the He II line in spectrum number 12. The histogram-like curve is the data from spectrum 12, the lower black curve the background as taken from spectrum 1. The upper black curve is the fit to the data and the dotted lines are the two Gaussians (with respect to the background).

Table 6. Best-fit line fluxes for the two He II lines in 10^{-16} erg s^{-1} cm^{-2}.

No.	3203 Å	4685 Å 1st	4685 Å 2nd	ratio 1[1]	ratio 2[2]
11	2.4 ± 0.4	1.6 ± 0.7	15.8 ± 1.6	0.10 ± 0.04	0.14 ± 0.03
12	4.3 ± 0.5	5.6 ± 1.2	25.1 ± 1.6	0.22 ± 0.05	0.14 ± 0.02

[1] Flux ratio between the two components of the line at 4685 Å; [2] flux ratio between both components of the 4685 Å line and the 3203 Å line.

6. Discussion

Stars of spectral type M5–M6 are located at the boundary between early M dwarfs and late M dwarfs. Among the former, very strong X-ray emitters exhibiting more or less permanent flaring (Robrade & Schmitt 2005) are found, while the latter are often – in quiescence – hardly detectable as X-ray sources, yet these stars somehow have the ability to produce enormous enhancements in X-ray luminosity (as well as chromospheric and transition region radiation) during flares (Rutledge et al. 2000; Schmitt & Liefke 2002; Stelzer et al. 2006). In this context, CN Leo behaves according to expectations. Its X-ray luminosity is lower than what is observed for late-type stars with spectral type M3/M4 or earlier; the more or less continuous flaring observed for these stars is replaced by either quiescent periods or well-identified individual flares, while only some low-amplitude flickering is left of the continuous variability of earlier M dwarfs.

The example of Proxima Cen (Güdel et al. 2002a, 2004), however, shows that the flares observed for such "intermediate" objects can also reach very large amplitudes.

CN Leo's coronal temperature is lower than the coronal temperatures typically found for earlier M-type dwarfs (Robrade & Schmitt 2005). A temperature component in excess of 20 MK as found in the more active, earlier M dwarfs (Stelzer et al. 2002; Robrade & Schmitt 2005) could not be detected in CN Leo; instead a persistent 2 MK cool component was found in addition to a dominant 7 MK temperature component. The coronal densities obtained for CN Leo are low and hardly distinguishable from the low-density limit, consistently fitting the picture of typical stellar coronae as investigated by Ness et al. (2003). Density variations related to different states of activity, as found by Maggio & Ness (2005), are consistent with the data, but remain speculative due to large measurement errors; clearly, much higher signal-to-noise is required for a definite measurement.

Stellar coronae often exhibit distinct abundance anomaly patterns. Only a few comparably inactive stars show a solar (photospheric) like coronal abundance pattern or even a FIP effect as observed on the Sun, with low first ionisation potential elements like iron enhanced by factors greater than two. Instead, especially very active stars exhibit the reverse pattern with the low-FIP elements being depleted and high-FIP elements enhanced. As a result, the metallicity in active stellar coronae is often low in general. These findings apply to active M dwarfs in particular and clear evidence for an inverse FIP effect has been found among early M dwarfs with respect to solar photospheric abundances (e.g. Maggio et al. 2004; Robrade & Schmitt 2005). The occurrence of FIP and IFIP effects seems to be correlated with activity (Güdel et al. 2002b; Telleschi et al. 2005): the FIP effect turns into the inverse FIP effect and the inverse FIP effect becomes stronger with increasing activity. Thus one would only expect a moderate IFIP effect for stars with decreasing activity like CN Leo, which is precisely what is observed. We find the overall abundance level to be about solar, also fitting the picture of an increased metallicity contrary to the sub-solar level often observed for very active stars. However, since coronal abundance determinations are difficult for very late M dwarfs, it is not clear if and how these trends proceed for such objects.

Our simultaneous VLT/UVES and *XMM-Newton* measurements have shown that the evolution of the lower-temperature X-ray component can be traced well from the ground using the Fe XIII 3388 Å flux. The different X-ray activity levels observed on December 11th and 13th are also found in the Fe XIII data. Unfortunately the signal-to-noise of these data is such that short-term variations within a given night can be detected only with great difficulty. However, long-term variability with possibly larger amplitudes should be easily detectable. The accuracy of the cross-calibration between the ground-based Fe XIII 3388 Å and predictions based on X-ray measurements is at the moment roughly a factor of $\sim$2. A possible repetition of such simultaneous observations should provide a more careful flux calibration of the optical data. The uncertainty arising from incorrectly assumed atomic physics parameters is difficult to assess, so more measurements are needed to ascertain which errors actually dominate the error budget.

Simultaneous multiwavelength campaigns of late-type stars allow the behaviour of different layers of the stellar atmosphere and their interactions to be directly evaluated. In this context correlated variations in different spectral bands or line fluxes are of specific interest. Many previous multiwavelength observations of active M dwarfs cover radio and X-ray observations with a focus on flares and on coronal properties (e.g. Guedel et al. 1996; Smith et al. 2005) with the intent of testing for relations like the Neupert effect or coronal heating models in the chromospheric evaporation scenario. Only a few recent studies (Hawley et al. 2003; Osten et al. 2005, 2006) also include UV or optical spectroscopy to monitor chromospheric emission lines. However, there does not seem to be a definite universal correlation between the fluxes in the different spectral bands. Nor is there any correlation between individual line fluxes, line broadening or velocity shifts. For example, Hawley et al. (2003) confirm the occurrence of the Neupert effect from their observations of individual flares on AD Leo and also discuss chromospheric evaporation and coronal backwarming. On the other hand, Osten et al. (2005) find a lack of correlation between different spectral bands and reject the Neupert effect as "the only" explanation of the mutual observed variations. Similarly, Smith et al. (2005) observed flares in X-rays on five active M dwarfs with missing counterparts in the radio, and vice versa, and discuss possible explanations.

Comparing our CN Leo observations to these studies, our target CN Leo has the advantage of showing discrete flares and periods of quiescence instead of permanent flaring, which makes it easier to clearly correlate variations observed in the different bandpasses and individual emission lines.

We covered two small flares with our simultaneous X-ray and optical observations. However, an in-depth discussion of the timing data to verify or falsify the presence of the Neupert effect would require far higher count rates to reduce statistical uncertainties. The time resolution of the blue optical spectra, covering most of the chromospheric emission lines, is low considering the time scales of the flare variations themselves. It is thus difficult to determine the exact onset of line variations from these spectra. The red spectra provide a better-resolved time coverage but lack the multitude of chromospheric lines seen in the blue range. Chromospheric line emission is clearly correlated with X-ray emission, at least concerning the two flares on December 13th, if we consider the flux increase and line broadening observed towards the end of the December 11th observations as connected to the strong flare about 20 min later and not covered by the optical data anymore.

7. Summary and conclusion

Our simultaneous optical/X-ray observations verify CN Leo's status as a star of intermediate activity. Compared to earlier M dwarfs, its X-ray luminosity is lower, its coronal temperatures is dominated by cooler components, and the abundances lack a pronounced inverse FIP effect. CN Leo exhibits three different "quasi-quiescent" levels in X-rays during the observations, which are also clearly observed in the chromospheric lines in the optical. While the highest of these states on December 11th 2005 may be due to the tail of the decay phase of a long duration flare, there is no such obvious explanation for the higher activity state on December 13th compared to the May 2004 observation. Since the X-ray flux in the 2004 observation is comparable to the lowest X-ray luminosity measured by *ROSAT*, we regard this state as the true quasi-quiescent level of CN Leo.

We find coronal densities from the O VII triplets $n_\mathrm{e} \sim 10^{10}$ cm^{-3}, while the Ne IX measurements are consistent with the low-density limit. During the flare on the second night, we also measured transition region densities from two He II lines that also give $n_\mathrm{e} \sim 10^{10}$ cm^{-3}.

The line flux of the forbidden ultraviolet Fe XIII line at 3388 Å varied only a little during our observations, and the observed flux level is slightly lower on the second night compared to the first night. Variations in both the X-ray lines produced at similar coronal temperatures and in the emission measure of the cool 2 MK component agree well with the Fe XIII line flux, all turn out to be quite stable and did not vary at all, even during the onset of a flare in the second night. A line shift towards bluer wavelengths is indicated by the line fit (but within the errors the wavelength is in agreement with the rest wavelength). Such a line shift for the forbidden Fe XIII line during a short duration flare has been noticed before (Fuhrmeister et al. 2004) and would also be expected, as hot material is often shifted upwards or even ejected during flares. In general our observations show that the Fe XIII line is a good indicator of the behaviour of the cool coronal temperature component of CN Leo, whose status and whose variations can thus be diagnosed from ground-based observations alone from the relative variations in the Fe XIII 3388 Å line fluxes. The agreement between the "predicted" and observed absolute Fe XIII 3388 Å line fluxes is currently about a factor of 2, and it is unclear which errors dominate the error budget.

Acknowledgements. CHIANTI is a collaborative project involving the NRL (USA), RAL (UK), MSSL (UK), the Universities of Florence (Italy) and Cambridge (UK), and George Mason University (USA).

B.F. and C.L. acknowledge financial support by the DLR under 50OR0105.

References

Anders, E., & Grevesse, N. 1989, Geochim. Cosmochim. Acta, 53, 197
Arnaud, K. A. 1996, in Astronomical Data Analysis Software and Systems V, ed. G. H. Jacoby, & J. Barnes, ASP Conf. Ser., 101, 17
Audard, M., Güdel, M., & Skinner, S. L. 2003a, ApJ, 589, 983
Audard, M., Güdel, M., Sres, A., Raassen, A. J. J., & Mewe, R. 2003b, A&A, 398, 1137
Brinkman, A. C., Behar, E., Güdel, M., et al. 2001, A&A, 365, L324
Crespo-Chacón, I., Montes, D., García-Alvarez, D., et al. 2006, A&A, 452, 987
Fuhrmeister, B., Schmitt, J. H. M. M., & Wichmann, R. 2004, A&A, 417, 701
Fuhrmeister, B., Schmitt, J. H. M. M., & Hauschildt, P. H. 2005a, A&A, 436, 677
Fuhrmeister, B., Schmitt, J. H. M. M., & Hauschildt, P. H. 2005b, A&A, 439, 1137
Gabriel, A. H., & Jordan, C. 1969, MNRAS, 145, 241
Güdel, M., Audard, M., Skinner, S. L., & Horvath, M. I. 2002a, ApJ, 580, L73
Güdel, M., Audard, M., Sres, A., et al. 2002b, in Stellar Coronae in the Chandra and XMM-NEWTON Era, ed. F. Favata, & J. J. Drake, ASP Conf. Ser., 277, 497
Güdel, M., Audard, M., Reale, F., Skinner, S. L., & Linsky, J. L. 2004, A&A, 416, 713
Guedel, M., Benz, A. O., Schmitt, J. H. M. M., & Skinner, S. L. 1996, ApJ, 471, 1002
Hawley, S. L., Allred, J. C., Johns-Krull, C. M., et al. 2003, ApJ, 597, 535
Henry, T. J., Subasavage, J. P., Brown, M. A., et al. 2004, AJ, 128, 2460
Kirkpatrick, J. D., Henry, T. J., & McCarthy, D. W. 1991, ApJS, 77, 417
Landi, E., Del Zanna, G., Young, P. R., et al. 2006, ApJS, 162, 261
Liefke, C., & Schmitt, J. H. M. M. 2007, in preparation
Maggio, A., & Ness, J.-U. 2005, ApJ, 622, L57
Maggio, A., Drake, J. J., Kashyap, V., et al. 2004, ApJ, 613, 548
Mitra-Kraev, U., Harra, L. K., Güdel, M., et al. 2005, A&A, 431, 679
Mohanty, S., & Basri, G. 2003, ApJ, 583, 451
Ness, J.-U., & Wichmann, R. 2002, Astron. Nachr., 323, 129
Ness, J.-U., Schmitt, J. H. M. M., Burwitz, V., et al. 2002, A&A, 394, 911
Ness, J.-U., Audard, M., Schmitt, J. H. M. M., & Güdel, M. 2003, Adv. Space Res., 32, 937
Osten, R. A., Hawley, S. L., Allred, J. C., Johns-Krull, C. M., & Roark, C. 2005, ApJ, 621, 398
Osten, R. A., Hawley, S. L., Allred, J., et al. 2006, ApJ, 647, 1349
Pavlenko, Y. V., Jones, H. R. A., Lyubchik, Y., Tennyson, J., & Pinfield, D. J. 2006, A&A, 447, 709
Piskunov, N. E., & Valenti, J. A. 2002, A&A, 385, 1095
Pradhan, A. K., & Shull, J. M. 1981, ApJ, 249, 821
Reid, I. N., Hawley, S. L., & Gizis, J. E. 1995, AJ, 110, 1838
Robrade, J., & Schmitt, J. H. M. M. 2005, A&A, 435, 1073
Rutledge, R. E., Basri, G., Martín, E. L., & Bildsten, L. 2000, ApJ, 538, L141
Schmitt, J. H. M. M., & Liefke, C. 2002, A&A, 382, L9
Schmitt, J. H. M. M., & Liefke, C. 2004, A&A, 417, 651
Schmitt, J. H. M. M., & Wichmann, R. 2001, Nature, 412, 508
Smith, K., Güdel, M., & Audard, M. 2005, A&A, 436, 241
Smith, R. K., Brickhouse, N. S., Liedahl, D. A., & Raymond, J. C. 2001, in Spectroscopic Challenges of Photoionized Plasmas, ed. G. Ferland, & D. W. Savin, ASP Conf. Ser., 247, 161
Stelzer, B., Burwitz, V., Audard, M., et al. 2002, A&A, 392, 585
Stelzer, B., Schmitt, J. H. M. M., Micela, G., & Liefke, C. 2006, A&A, 460, L35
Telleschi, A., Güdel, M., Briggs, K., et al. 2005, ApJ, 622, 653
Wallerstein, G., & Tyagi, S. 2004, PASP, 116, 554